Systematic changes in serpentine Si isotope signatures across the Mariana forearc – a new proxy for slab dehydration processes

Sonja Geilert [a],[*], Elmar Albers [b], Daniel A. Frick [c], Christian T. Hansen [b],
Friedhelm von Blanckenburg [c],[d]

[a] GEOMAR Helmholtz Centre for Ocean Research Kiel, Wischhofstr. 1-3, 24148 Kiel, Germany
[b] MARUM – Center for Marine Environmental Sciences, University of Bremen, Leobener Str. 8, 28359 Bremen, Germany
[c] GFZ German Research Centre for Geosciences, Telegrafenberg, 14473 Potsdam, Germany
[d] Department of Earth Sciences, Institute of Geological Sciences, Freie Universität Berlin, Malteserstr. 74-100, 12249 Berlin, Germany

A B S T R A C T

The Mariana forearc is a unique location for exploring the role serpentinization plays in the marine Si cycle by means of Si stable isotope variations. Here, active mud volcanism transports deep, serpentinized mantle wedge material to the surface and thus offers a natural window to slab dehydration processes in dependence of changing temperature and pressure with depth. Si isotopes were measured *in situ* by femtosecond laser ablation MC-ICPMS in serpentine within ultramafic clasts from three mud volcanoes (Yinazao, Fantangisña, and Asùt Tesoru) sampled during International Ocean Discovery Program Expedition 366. To corroborate the results, serpentinization of olivine was studied in batch experiments. The Si isotope ratios show large variations between the mud volcanoes and between individual serpentine generations within a given mud volcano. Serpentine that formed early under low water/rock ratios exhibits δ^{30}Si of -0.41 ± 0.04‰ (1SD) similar to unaltered olivine which agrees well with experimental findings predicting no significant isotope fractionation during early serpentinization. In contrast, late serpentine veins formed under higher water/rock ratios span a wide range of Si isotope ratios that differ significantly between the individual mud volcanoes. With increasing distance to the trench, δ^{30}Si of late veins are -0.10 ± 0.07‰, -1.94 ± 0.13‰, and -0.80 ± 0.22‰ and -0.93 ± 0.21‰. These δ^{30}Si values are interpreted to record the isotopic composition of the fluid source, namely subducted biogenic silica and pore fluids, clays, and altered oceanic crust that dehydrate as consequence of rising pressure and temperature with depth. We show that Si isotopes of mantle wedge serpentinites can be used as a reliable new proxy for slab dehydration processes. They may be used in paleo-forearc systems to unravel oceanic sediment and silica biomineralization evolution through geological time.

© 2021 The Authors. Published by Elsevier B.V. This is an open access article under the CC BY license (http://creativecommons.org/licenses/by/4.0/).

1. Introduction

The global silicon (Si) cycle is of interest in many research areas. Si is a key nutrient in the ocean controlling primary production and is closely linked to the carbon cycle in weathering reactions that control climate feedbacks (e.g. Tréguer et al., 2021). A marine process that has until now gained particularly little attention with regard to the geochemical cycling of Si is serpentinization, which describes the transformation of mantle peridotite into hydrated ultramafic rock in diverse oceanic settings. This research gap persists even though serpentinization environments have been recognized as sinks for Si (Frost and Beard, 2007), and serpentinization in gen-

eral plays a key role in global element cycling (e.g. Deschamps et al. (2013) and references therein). However, Si sources, migration pathways, and precipitation reactions during serpentinization are not fully disclosed and the role of serpentinization in the global Si cycle is thus still underconstrained (see recent reviews by Frings et al. (2016) and Sutton et al. (2018)).

Serpentine has in its structural formula a higher number of Si per mole Mg (or Fe) with 2 mole Si per 3 mole Mg (2/3 mole) than olivine (0.5 mole). This shortage in Si leads to generally low $a\mathrm{SiO_2}$ during the isochemical hydration of olivine (Frost and Beard, 2007) and, resulting from the excess in Mg, to the formation of brucite (e.g. Bach et al., 2006). When pyroxene (1 mole Si per mole Mg) participates in the reaction, $a\mathrm{SiO_2}$ is (locally) higher. The replacement of pyroxene by serpentine results in excess Si in the vicinity of the pyroxene grains which may allow the direct transformation of olivine into serpentine (e.g. Schwarzenbach et al., 2016).

In addition, Si may also be introduced to the system from external sources by the serpentinization fluids (e.g., fluids released from mafic rocks/sediments in the subducting slab; Kastner et al., 2014). Such metasomatism is, however, largely dependent on water/rock (w/r) ratios during serpentinization, i.e., the amount of fluid (carrying the external Si_{aq}) that reacts with each portion of rock. Theoretically, at very low w/r ratios (and hence very limited amounts of Si_{aq} that are added to the system), most of or all the Si_{aq} will be incorporated into serpentine so that no fractionation is expected. This assumption would be consistent with the observations by Wang et al. (2019), who detected no difference between silicon isotope signatures ($\delta^{30}Si$) of serpentinized peridotites and unreacted mantle peridotites. On the contrary, high w/r ratios may introduce more Si per portion of rock than what can be incorporated into serpentine - in which case isotopic change (and hence a change in bulk serpentinite $\delta^{30}Si$) appears reasonable.

In subduction zones, serpentinization of mantle wedge peridotite is triggered by fluids that are released from subducting sediments and/or from altered oceanic crust. Fluid release occurs as a response to rising pressure (P) and temperature (T) with depth and the associated mineral dehydration reactions (e.g. Hyndman and Peacock, 2003; Mottl et al., 2004). At forearc depths, such slab-derived fluids are generally thought to transport Si from the subducting slab into the overlying mantle wedge (Kastner et al., 2014).

One reason for the still incomplete knowledge of the processes entailing Si liberation from slab minerals and its incorporation into serpentinites is the inaccessibility of the forearc mantle wedge. A natural window into these mantle wedge processes at depth is offered by the active mud volcanism of the Mariana forearc that transports materials from the mantle wedge to the surface (Fryer et al., 1985). Earlier studies have shown that in particular across the Mariana forearc serpentinites and associated pore fluids record the geochemical reactions occurring at the slab-mantle interface. Systematic trends in reaction progress were reported in dependence of metamorphic gradients at depth (Mottl et al., 2004; Hulme et al., 2010). Recent studies by Kahl et al. (2015) and Albers et al. (2020) report chemical alteration of the deep-sourced fluids during their continued interaction with the mantle wedge, as based on fluid mobile element compositions of serpentinized ultramafic clasts recovered from the Mariana mud volcanoes.

Silicon stable isotopes can potentially provide fingerprints of these processes as they are sensitive to mineral dissolution and precipitation reactions. Si isotope ratios differ between minerals involved in slab dehydration reactions (e.g. opal, clays) and we propose that Si isotopes can represent a new proxy for fluid composition, sourced by slab mineral dehydration. The capacity of Si isotopes to record signals of subducted silicate materials offers the unique opportunity to assess the marine seafloor sedimentary composition in the geological past, by investigating the Si isotope signatures of serpentine in paleo forearcs. This new proxy will help to shed further light on the long-standing question when first Si-utilizing organisms evolved on Earth and/or provide information on Archean seawater composition.

To identify the sources of the serpentinization fluids we studied serpentinized ultramafic clasts from the Mariana forearc sampled during IODP Expedition 366 for their *in situ* micrometer-scale Si isotope compositions. Additionally, we experimentally simulated the serpentinization of olivine in batch experiments at 100, 200, and 300 °C (40 MPa), in order to study Si partitioning and isotope fractionation under controlled laboratory conditions. These results were used to investigate the process of fluid release into the mantle wedge and its potential to record changes in the oceanic Si cycle in the geological past.
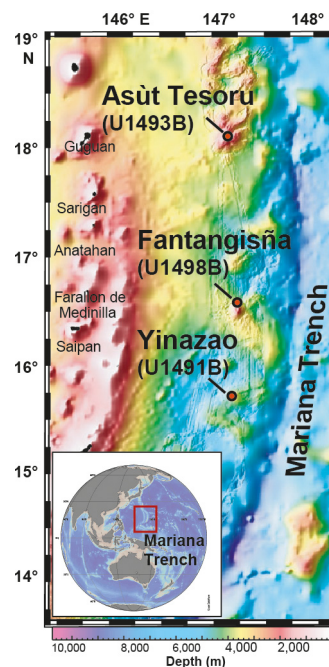
Fig. 1. Study area and locations of IODP Expedition 366 drill sites at the Yinazao, Fantangisña, and Asùt Tesoru mud volcanoes in the Mariana forearc region (modified after Fryer et al., 2018). (For interpretation of the colors in the figure(s), the reader is referred to the web version of this article.)

2. Geological background and sample description

The Mariana convergent plate margin is a non-accretionary subduction system, in which the Pacific Plate descends beneath the Philippine Sea Plate. Water released from the subducting slab enters the mantle wedge and converts the peridotite to serpentine minerals. Deep faults in the forearc lithosphere allow these fluids and the low-density serpentinite materials to buoyantly rise to the seafloor, where they form a number of vast serpentinite mud volcanoes up to 30 km in diameter and 2 km in height (e.g. Fryer et al., 1985). Between individual mud volcanoes across the forearc, systematic changes of the chemical composition of these fluids were interpreted to reflect changing diagenetic and metamorphic conditions of the subducting slab (Mottl et al., 2004; Hulme et al., 2010). With increasing distance to the trench (and thus increasing T and P at the slab–wedge interface), increasing Na/Cl, B, Rb, Cs, light REE (LREE) and decreasing Ca, Sr, and Y concentrations were interpreted as sediment compaction, carbonate dissolution, and opal diagenesis at 30 to 80 °C (∼5-14 km slab depth), expulsion of interlayer water and clay diagenesis at 80 to 150 °C (∼14-18 km slab depth), and fluid freshening and decomposition of clays and altered oceanic crust (AOC) at >250 °C (≥18 km slab depth) (Mottl et al., 2004; Hulme et al., 2010; Fryer et al., 2018). Also fluid-mobile-element (FME) contents in serpentine in ultramafic clasts were found to mimic the above mentioned slab dehydration processes (Kahl et al., 2015; Albers et al., 2020).

Samples investigated in this study originate from Yinazao, Fantangisña, and Asùt Tesoru serpentinite mud volcanoes that were drilled during IODP Expedition 366 (Fig. 1; Fryer et al., 2018). These mud volcanoes are thought to sample slab-depths of 13, 14, and 18 km with corresponding slab temperatures of about 80 °C, 150 °C, and 250 °C, respectively (Oakley et al., 2007; Fryer et al., 2018). Three variably serpentinized ultramafic clasts, one from each mud volcano, were investigated in this study. Two clasts are dunitic (samples U1491B-5H-CC, 0–3 cm, from Yinazao and U1498B-4R-1, 94–97 cm, from Fantangisña) and one is harzburgitic in composition (sample U1493B-9X-CC, 14–16 cm, from Asùt

Tesoru). The samples show evidence for several individual serpentine vein generations. A detailed description of the microfabrics can be found in section 5.1.

3. Batch experiments on olivine serpentinization

Silicon partitioning and the associated isotope fractionation during serpentinization of olivine were investigated in batch experiments at three different temperatures, 100, 200, and 300 °C and at a pressure of 40 MPa. We reacted 5 g olivine powder with 75 ml of a deoxygenated artificial seawater-like fluid (3.2 wt-% NaCl) to simulate closed-system serpentinization. A detailed description of the experimental setup can be found in Hansen et al. (2017) and references therein. In brief, the reactants were placed in a flexible gold reaction cell that is confined inside a stainless steel pressure vessel (Parr Instruments). The reaction fluid was repeatedly sampled by utilizing a titanium valve connected to a titanium capillary tube that extended into the reaction cell. The fluids were filtered through an in-line titanium frit (2 µm, Vici). At all times, reactants were exclusively in contact with gold or passivated titanium.

For the olivine powder reactant pure, translucent, and inclusion free peridotite-derived crystals (Ø 3-5 mm, Pakistan) were ground in an agate mortar and wet-sieved to grain sizes between 50-100 µm. The 3.2 wt-% NaCl solution was prepared from suprapure sodium chloride (Merck®) and ultrapure water (MilliQ®). Oxygen was removed through prolonged bubbling of the fluid with N_2. Consecutive fluid samples were characterized for pH, salinity, and major element chemistry. Solid reaction products were sampled and characterized (minerology, mineral chemistry) at the end of the experiments. The experiments were terminated when steady-state conditions in the fluid chemistry were reached.

4. Analytical methods

4.1. Electron microprobe

SiO_2, FeO, and MgO concentrations of primary and secondary phases were determined with a CAMECA SX100 microprobe at the University of Bremen. The device is equipped with four wavelength dispersive spectrometers. Analytical conditions included accelerating voltages of 15 kV and beam currents of 10 nA. Peak counting times were 40 s per element and analyses were carried out with a defocused beam (10 µm). The built-in PAP correction was applied for data reduction and correction. Replicate analyses of olivine standard no. NMNH 111312-44 from the Smithonian Institution, Washington D.C., were used to check data quality (number of analyses = 30). The external reproducibility is 0.6% for SiO_2, 1.6% for FeO, and 0.5% for MgO, and the averaged relative uncertainties as a measure for accuracy are 1.1%, 3.3%, and 0.1%, respectively.

4.2. Laser ablation MC-ICPMS of the serpentinites

In situ silicon isotope ratios were measured at the GeoForschungsZentrum in Potsdam using a custom-built deep-UV (196 nm) femtosecond laser ablation system (GFZ fem2, containing a frequency-quadrupled Spectra Physics Solstice femtosecond laser, see Schuessler and Von Blanckenburg (2014) for technical details) coupled to an inductively coupled plasma multi-collector mass spectrometer (Thermo Fisher Scientific Neptune MC-ICP-MS, equipped with the Neptune Plus Jet Interface). The laser ablation paths were adapted to the irregular shapes of veins, placing the paths such that they sampled pure phases as identified by optical inspection. The laser spot (ca. 25 µm in diameter) was continuously scanned along these paths, typically ten times, for a total ablation time of 100 s. The intensity between samples and standard was matched by adjusting the laser frequency (pulse repetition rate) from 15 Hz to 125 Hz. The laser and ICP-MS settings can

be found in Tables A.1 – A.3. Details regarding the instrumentation and evaluation of the data can be found in the appendix in Tables A.4 and A.5.

Instrumental mass bias was corrected by standard-sample-bracketing using NBS28 as measurement standard. The Si isotope results are reported in the δ-notation as permil deviation relative to NBS28 (quartz NIST SRM8546 alias NBS28, $\delta^{29}Si \equiv 0$ and $\delta^{30}Si \equiv 0$):

$$\delta^{30}Si = \left[\frac{\left(\frac{^{30}Si}{^{28}Si}\right)_{sample}}{\left(\frac{^{30}Si}{^{28}Si}\right)_{NBS28}} - 1 \right] [in \text{ ‰}] \tag{1}$$

In all three analytical sessions, BHVO-2 and GOR132G reference materials were repeatedly analyzed. There is a good agreement between the in situ determined isotope ratios and the literature values; Table A.4 and A.5). Samples 104-93-x to 130-93-x (with x as the sample ID) may have been associated with higher uncertainties due to imperfect ion beam stability during measurements (see Table A.4 for details).

4.3. Si isotope measurements of the experimental samples

Solids from the experiments were decomposed for Si isotope measurements by NaOH digestion. Unreacted olivine, final reaction products, and the reference standard BHVO-2 were digested using a modified method of van den Boorn et al. (2006). About 30 mg of $NaOHxH_2O$ (≥99.99% suprapur, Merck) was added to about 1 mg of the pulverized solid and placed on a hot plate at 100 °C for 3 days. Then, the sample-$NaOHxH_2O$ mix was re-dissolved in 1 ml Milli-Q (MQ) water and centrifuged to separate solids from the supernatant. Subsequently, 100 µL 6M HNO_3 were added to the undissolved solid material and left on a hot plate for 1 hour. The solid residue was separated again from the supernatant by centrifugation, and again mixed with about 30 mg of $NaOHxH_2O$ and placed on a hot plate at 100 °C for three days. The sample-NaOH mix was re-dissolved with 1 ml MQ water. Si yield was > 97% and the procedure blank ≤0.7 µg Si.

The Si concentrations of the experimental fluids and digested solids were measured by photometry. For Si isotope measurements, the samples were chromatographically purified following a method of Georg et al. (2006). Before column separation, a pH of 2 was established with concentrated HNO_3. One ml of the samples with a concentration of about 140 µM Si were loaded onto pre-cleaned cation-exchange resins (Biorad AG50 W-X8) and subsequently eluted with two ml MQ water.

Si isotopes were measured on the NeptunePlus HR MC-ICPMS at GEOMAR in medium-resolution mode and wet-plasma conditions, using a Teflon spray chamber. The instrumental mass bias was controlled by Mg doping. The ^{28}Si intensity of a sample concentration of 30 µM Si was about 3 to 4 V and the MQ blank was ≤20 mV (blank/signal ratio ≤ 0.6%). All samples were measured using the standard-sample bracketing method. The reference materials yielded $\delta^{30}Si$ of -1.46 ± 0.09‰ (2SD; n=45) for IRMM018, $+1.25\pm0.10$‰ (2SD; n=34) for Diatomite, and -0.33 ± 0.13‰ (2SD; n=12) for BHVO-2. Solid and fluid samples were measured at least three times and their $\delta^{30}Si$ uncertainties ranged between 0.11 and 0.14 ‰ (2SD).

5. Results

5.1. Petrography

The ultramafic clasts are serpentinized to different degrees (serpentinization in sample U1491B-5H-CC, 0–3 cm, is ~60 vol% whereas the other two samples are completely altered) and show
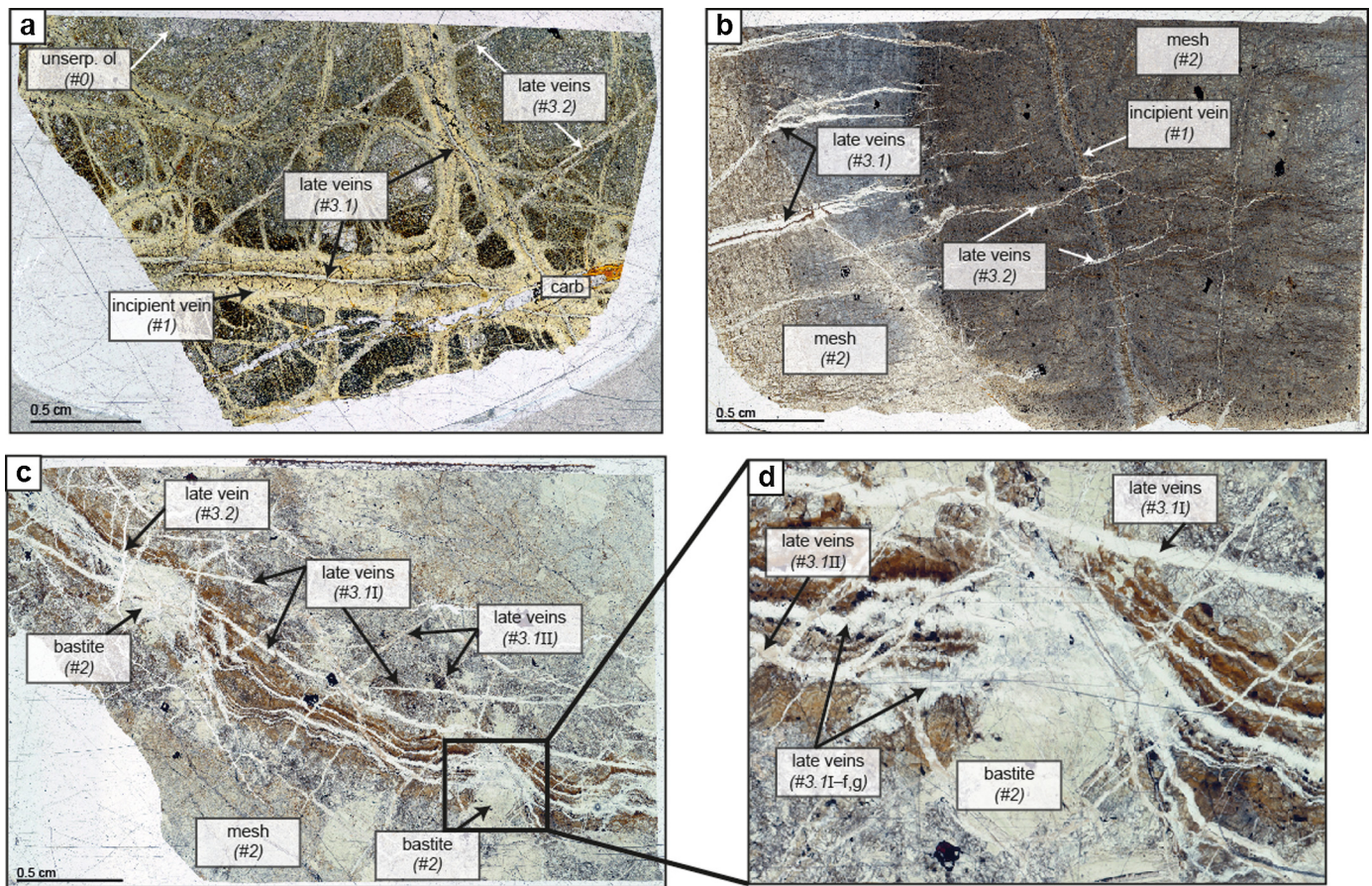
Fig. 2. Photomicrographs of the ultramafic clasts from (a) Yinazao, (b) Fantangisña, (c) Asùt Tesoru, and (d) close-up of late vein #3.1 cross-cutting the bastite present in the clast from Asùt Tesoru. Note that veins #3.1I-f,g cannot unequivocally be assigned to a vein generation (section 5.3.1). The veins are formed under different w/r ratios, which affect serpentine δ^{30}Si values (see text for details). Abbreviations: ol, olivine; carb, carbonate.

distinct microfabrics. Unserpentinized parts of the clasts are composed of fine-grained olivine and minor orthopyroxene and spinel (Fig. 2a). The secondary assemblages comprise serpentine, brucite, and minor amounts of magnetite, Fe-alloys, and sulfides. These assemblages as well as their microtextural relationships record distinct phases of serpentinization under different physicochemical conditions that resulted from the prolonged interaction with slab-derived fluids. Late phases such as iowaite and Ca carbonates (sample U1491B-5H-CC, 0–3 cm) formed during reaction with seawater after the emplacement of the clasts at the seafloor. General microfabrics and mineral chemical compositions are described and discussed in Albers et al. (2020) and are in line with earlier studies on serpentinite clasts from the Mariana forearc (e.g. Kahl et al., 2015; Debret et al., 2019).

In detail, the polyphase serpentinization history of the clasts is preserved by the occurrence of several generations of serpentine (# indicates sequence of formation), the relative timing of the formation sequence can be determined on the basis of vein crosscutting relationships (Fig. 2). Transgranular 'incipient' veins that consist of serpentine, brucite, and minor magnetite record the first infiltration of fluids (#1; Fig. 2a,b). The formation of brucite, exclusively occurring in the centers of these veins, indicates the depletion of fluid Si during ongoing serpentinization and thus rather low water/rock (w/r) ratios. In the Yinazao-clast, these veins were locally reactivated and provided pathways for further fluid flow and visually distinct vein centers (Fig. 2a). This early vein formation was followed by fluid flow along narrower veinlets and grain boundaries and by the pervasive serpentinization of olivine and orthopyroxene (#2). These replacements are preserved in mesh and hourglass (serpentinized olivine) as well as in bastite textures (serpen-

tinized pyroxene) (Fig. 2b-d). The pervasive alteration presumably records the stage in which the lowest volumes of fluid participated in the reactions and the conditions were mostly rock-dominated and the w/r ratios were lowest. These fabrics are crosscut by a randomly-oriented generation of veins that consists of pure serpentine and likely formed in an anisotropic stress regime (Fig. 2; #3.1). Serpentine in these veins shows no direct interaction with its host minerals (e.g. Fig. 2a) and the veins have been interpreted as having formed in the presence of larger amounts of fluids, and thus rather high w/r ratios, which have not necessarily been in (local) chemical equilibrium with the host minerals. Note that in Asùt Tesoru, there are two generations (#3.1I and #3.1II) of this kind, #3.1II crosscutting #3.1I (Fig. 2c,d). This vein generation is overprinted by even younger veins that differ in appearance through the samples (#3.2). In the Yinazao-sample, fluids migrated through preexisting pathways in a rather pervasive manner (Figs. 2a); thus interaction of the fluid with the host minerals occurred and are interpreted to have formed under rather low w/r ratios. In the clast from Asùt Tesoru, by contrast, the latest vein generation likely formed under similarly high w/r conditions compared to the veins of #3.1 as its mineral assemblage and optical appearance are remarkably similar to those of veins #3.1 (Figs. 2c).

On the basis of the above described textural relationships, we classified the different serpentine occurrences as three distinct generations; these are (1) serpentine in incipient veins that formed under rock-dominated conditions (#1; low w/r ratio), (2) pervasive serpentinization emanating from incipient veins, producing mesh and bastite textures (#2; lowest w/r ratio), and (3) serpentine in late veins, most of which formed under fluid-dominated conditions
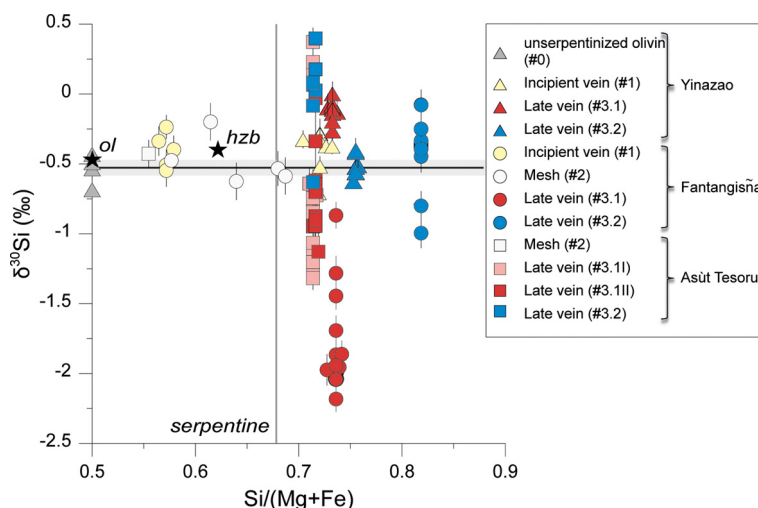
Fig. 3. The δ^{30}Si values versus the Si/(Mg+Fe) ratios of unserpentinized olivine, mesh, and different vein generations (#) for Yinazao, Fantangisña, and Asùt Tesoru serpentinites. Note that average Si/(Mg+Fe) ratios of veins from the same generation were taken for samples where no major element data was available. For unserpentinized olivine and mesh in the Yinazao-clast, the Si/(Mg+Fe) ratios were taken from Albers et al. (2020). Black horizontal line is the average of unserpentinized olivine with -0.52 ± 0.11‰ (1SD, gray area). Reference values for olivine (ol; δ^{30}Si $= -0.44$‰; Savage et al., 2011), harzburgite (hzb) with a composition of 85% olivine, 10% Orthopyroxene, and 5% clinopyroxene (δ^{30}Si $= -0.37$‰; Savage et al., 2010), and serpentine are shown for comparison.

and in which the serpentine precipitated in void space (#3.1 and #3.2; high w/r ratio).

5.2. Serpentine major element composition

Throughout the three mud volcanoes, the different generations of serpentine show a narrow range of Si-Mg-Fe composition. Of all serpentine analyses, 90% are within X_{Mg} = Mg/(Mg+Fe) of 0.92–0.96 and 84% are within Si/(Mg+Fe) of 0.6–0.73 and hence close to ideal serpentine, i.e., $(Mg,Fe)_3Si_2O_5(OH)_4$, with Si/(Mg+Fe) of 0.67 (Fig. 3; Table A.6). Thus, our data show no indication of intergrowth with other phases such as brucite ($Mg(OH_2)$) but are instead representative of pure serpentine.

5.3. Silicon isotope compositions

5.3.1. Mariana forearc serpentinites and olivine samples

Individual measurement locations and related δ^{30}Si are shown in photomicrographs of the ultramafic clasts from Yinazao, Fantangisña, and Asùt Tesoru in the supplement (Fig. A.1-A.3).

Unserpentinized olivine (#0) in the clast from Yinazao mud volcano yields an average δ^{30}Si of -0.52 ± 0.11‰ (n=4; 1SD) (Fig. 3; Table 1, A.6). This result is similar to previously determined values of olivine of on average -0.44 ± 0.02‰ (Savage et al., 2011). The average δ^{30}Si of the mesh serpentine (#2) is -0.47 ± 0.17‰ (n=5; 1SD) for Fantangisña, and -0.41 ± 0.10‰ (n=1; measurement uncertainty is 2SE of line scan) for Asùt Tesoru (Fig. 3; Table 1, A.6).

Si isotopic compositions within individual veins are very homogeneous. Different serpentine veins in the Yinazao sample range in δ^{30}Si between -0.69 ± 0.10‰ and $+0.02 \pm 0.08$‰, those from Fantangisña show an even larger δ^{30}Si range between -2.17 ± 0.09‰ and -0.06 ± 0.09‰, and serpentine in veins from Asùt Tesoru varies between -1.30 ± 0.10‰ and $+0.41 \pm 0.17$‰ (Fig. 3). Indicated uncertainties refer to 2SE of the measurements (Table 1, A.6).

Average Si isotope values of the vein generations defined in section 5.1 are as follows (Table 1). Average δ^{30}Si for incipient veins (#1) are -0.36 ± 0.13‰ and -0.39 ± 0.13‰ for Yinazao and Fantangisña, respectively. Late veins of generation #3.1 yield δ^{30}Si of -0.10 ± 0.07‰ for Yinazao, -1.94 ± 0.13‰ for Fantangisña, and -0.93 ± 0.21‰ (#3.1I) and -0.80 ± 0.22‰ (#3.1II) for Asùt Tesoru. Late veins of generation #3.2 yield δ^{30}Si of -0.49 ± 0.08‰

for Yinazao, -0.30 ± 0.12‰ for Fantangisña, and $+0.22 \pm 0.19$‰ for Asùt Tesoru (uncertainty is 1SD; Table 1, A.6). Note that late veins #3.1I-f and $-g$ in the Asùt Tesoru sample cannot unequivocally be assigned to a vein generation since their δ^{30}Si deviate from apparently corresponding generation #3.1I and rather overlap with generation #3.2. Similarly, bastite measurements (#2b, c) show a large range in δ^{30}Si values between -0.61‰ and $+0.10$‰ and deviate from the mesh value at Asùt Tesoru (-0.41‰). Bastite δ^{30}Si are likely influenced by crosscutting veins (Fig. 2d) und cannot unequivocally be assigned to a vein generation.

5.3.2. Batch experiments on olivine serpentinization

The fluids of the 100, 200, and 300 °C experimental runs were sampled in regular intervals to monitor fluid evolution. The system attained steady-state in terms of major element chemistry, pH, and salinity after 222, 224, and 152 days for the 100, 200, and 300 °C experimental runs, respectively (Hansen et al., 2017; Schlicht, 2020). Fluid Si concentrations, resulting exclusively from olivine dissolution, initially increased to 139 μM and then decreased to 29 μM (Table 2).

Characterization of the solids retrieved after termination of the experiments showed that the reaction product was strongly altered compared to the initial olivine in all three experimental runs (Hansen et al., 2017; Schlicht, 2020). Most of the olivine had reacted to fine needles of serpentine (chrysotile) as well as brucite and magnetite. Such final mineral assemblages can also be found in natural serpentinite assemblages and are in line with thermodynamic modeling data (Hansen et al., 2017), thus confirming the applicability of the experiments to represent serpentinization environments. The fluid-rock exchange rates can be calculated by the reaction turnover (RT) of the experiment. As serpentine is the sole product mineral incorporating Si, the absolute amount of reacted olivine and hence RT in the experiment can be derived from simple stoichiometric considerations, in that two moles of serpentine ($n_{serpentine}$) corresponds to one mole of olivine ($n_{olivine}$):

$$RT \ (mol\%) = \left(\frac{2 \cdot n_{serpentine}}{n_{olivine} + 2 \cdot n_{serpentine}} \right) \cdot 100 \qquad (2)$$

Following equation (2), RT are 12%, 69%, and 73% for the 100, 200, and 300 °C experimental runs, respectively (for a de-

Table 1

Average Si isotope values per serpentine generation of mesh and bastite textures and in veins. The generation and relative water/rock ratios (w/r ratio) are indicated based on the petrography of the ultramafic clasts (section 5.1). The label refers to the individual vein generations (Fig. 2 and section 5.1).

Phase	Generation	w/r ratio	Label	n[a]	Average δ^{30}Si per generation (‰)	1SD (‰)
Yinazao (U1491B-5H-CC)						
unserpentinized olivine	0	/	0-a,b	4	−0.52	0.11
incipient vein	1	low	1-a to c	10	−0.36	0.13
late vein	3	high	3.1-a to c	9	−0.10	0.07
late vein	3	low	3.2-a, b	7	−0.49	0.08
Fantangisña (U1498B-4R-1)						
incipient vein	1	low	1	5	−0.39	0.13
mesh	2	low	2-a to c	5	−0.47	0.17
late vein	3	high	3.1-a to d	10	−1.94	0.13
late vein	3	low	3.2-a to e	7	−0.30	0.12
Asùt Tesoru (U1493B-9X-CC)						
mesh	2	low	2-a	1	−0.41	0.10[b]
veins in bastite	not identifiable	high	2-b	2	0.09	0.01
	not identifiable	high	2-c	2	−0.34	0.39
late vein	3	high	3.1I-a to e	17	−0.93	0.21
late vein	not identifiable	high	3.1I-f,g	3	0.27	0.11
late vein	3	high	3.1II-a to h	12	−0.80	0.22
late vein	3	high	3.2	3	0.22	0.19

[a] Number of individual measurements per generation.
[b] Error equals standard error of measurement.

tailed evaluation of the serpentinization reactions see Hansen et al. (2017) and Schlicht (2020)).

The δ^{30}Si of the olivine reactant is -0.32 ± 0.13‰ and the solid product after the reaction was completed at $300\,°C$ has a δ^{30}Si of -0.22 ± 0.13‰ (Table 2). The δ^{30}Si of the solid products of the $100\,°C$ and $200\,°C$ experiments are -0.51 ± 0.11‰ and -0.25 ± 0.14‰, respectively.

Fluid samples from the $300\,°C$ experiment provided additional information on the Si partitioning and isotope fractionation process (note that fluid quantities from the 100 and $200\,°C$ experiments were too small Si isotope measurements). δ^{30}Si of the cool seawater-like fluid reactant is -0.82 ± 0.07‰ (pH$_{\text{in situ}}$ = 5.0) and increased rapidly to $+1.51 \pm 0.04$‰ upon heating (pH = 5.5). At the end of experiments, after attaining a steady state with respect to the fluid chemistry (152 days), δ^{30}Si returned to somewhat ^{30}Si-depleted values at -0.05 ± 0.07‰ (2SD) (Fig. 4a). This change in isotopic composition coincided with rising and falling silica activities in the initial and final stage of the experiment, respectively (Fig. 4b; Table 2).

6. Discussion

In the following, the δ^{30}Si values of the different vein generations are discussed in the context of rock- versus fluid-dominated systems, mineral dehydration reactions, and their potential as a new proxy to unravel the occurrence and evolution of siliceous organisms in the geological past.

6.1. Incipient veins (#1; low w/r ratio)

Serpentine in incipient veins (low w/r ratio) identified in Yinazao and Fantangisña features an average δ^{30}Si of -0.37 ± 0.13‰ (Fig. 3, 5), which is similar within uncertainty to unserpentinized olivine at Yinazao (-0.52 ± 0.11‰) and to olivine literature data (-0.44 ± 0.02‰ (1SD); Savage et al., 2011). We hence conclude that the Si isotopic composition of the mantle wedge peridotite was not significantly changed during the incipient serpentinization event. This can likely be attributed to the low w/r ratios characterizing the early hydration of the mantle wedge, i.e., to the fact that the amount of Si added to a given rock volume was minor and thus δ^{30}Si of the primary rock dominates.

6.2. Pervasive serpentinization and experimental results (#2; lowest w/r ratio)

The δ^{30}Si of mesh serpentine are similar between Fantangisña and Asùt Tesoru seamounts with on average -0.46 ± 0.15‰ (n=6; 1SD) (Fig. 3, 5). This value overlaps with unserpentinized olivine (#0) from Yinazao and the incipient serpentine veins (#1). Hence, a significant shift in Si isotopic composition during alteration of the ultramafics at low w/r ratios is not discernible. The protoliths' Si isotope values remain unchanged during pervasive serpentinization. This is in line with the conclusion made in the preceding paragraph in that serpentine in incipient veins, equally formed under low w/r ratios, resemble the δ^{30}Si of the primary rock. Consequently, the bulk composition of the mantle wedge did not markedly change at this stage.

The results of the serpentinization experiments at $300\,°C$ and $200\,°C$ are best compared to the pervasive serpentinization (#2; Fig. 3, 4) given that in these about 73% and 69% of the olivine, respectively, reacted to a serpentine product mineral assemblage. The δ^{30}Si of the reaction product at $300\,°C$ (serpentinized olivine) and the unreacted olivine are -0.22‰ and -0.32‰, respectively (Fig. 4a,b; Table 2), resulting in a Si isotope fractionation of Δ^{30}Si$_{\text{product-olivine}}$ = 0.10 ± 0.19‰ (1SD$_{\text{propagated uncertainty}}$), with Δ^{30}Si$_{\text{product-olivine}}$ = δ^{30}Si$_{\text{product}}$ (reaction product) - δ^{30}Si$_{\text{olivine}}$ (unreacted olivine). The Δ^{30}Si$_{\text{product-olivine}}$ at $200\,°C$ is 0.07 ± 0.19‰. These results are in line with literature data, which showed in experimental and theoretical predictions that Δ^{30}Si$_{\text{product-olivine}}$ decreases with increasing temperature and tends towards 0‰ at about $T > 80\,°C$ (Fig. 4c).

The reaction product of the $100\,°C$ experiment has a Δ^{30}Si$_{\text{product-olivine}}$ of -0.19 ± 0.18‰, slightly larger than the Si isotope fractionation at higher temperatures. Unfortunately, due to the large uncertainty no conclusions can be drawn if this Δ^{30}Si$_{\text{product-olivine}}$ is caused by the lower temperature or the low reaction turnover (12%). Within uncertainty all experimental results are thus almost identical to the unreacted olivine. Consequently, the experimental results are in agreement with the interpretation of the incipient veins and pervasive serpentinization (section 6.1 and above) that no significant Si isotope fractionation occurs at steady state. This is also in line with results by Wang et al. (2019) who found no significant Si isotope change between ser-

Table 2
Experimental conditions, fluid Si concentrations, and fluid and solid Si isotope values.

Sample ID	Note	Time (days)	pH$_{in\ situ}$	Si (μM)	log aSiO$_2$ (aq)	RT* (%)	Fluids δ^{29}Si (‰)	2SD (‰)	δ^{30}Si (‰)	2SD (‰)	Solids Sample ID	δ^{29}Si (‰)	2SD (‰)	δ^{30}Si (‰)	2SD (‰)	Δ^{30}Si$_{product-olivine}$ (‰)	1SD$_{prop.error}$ (‰)
HyLiB-01	starting solution	0	5	36	−7.6		−0.32	0.03	−0.82	0.07	unreacted ol	−0.14	0.09	−0.32	0.13	−	−
HyLiB-02	cool	0.1	5	39	−6.9		0.80	0.08	1.51	0.04	-	−	−	−	−	−	−
HyLiB-03	hot (300 °C)	0.2	5.5	138	−10.2	73	0.01	0.09	−0.05	0.07	-	−	−	−	−	−	−
HyLiB-09	hot (300 °C)	152	7.9	29		69					reaction product	−0.15	0.11	−0.22	0.13	0.10	0.19
	hot (200 °C)	224				12					reaction product	−0.13	0.10	−0.25	0.14	0.07	0.19
	hot (100 °C)	222									reaction product	−0.24	0.04	−0.51	0.11	−0.19	0.18

Data in italics from Hansen et al. (2017) and Schlicht (2020).
* RT denotes reaction turnover.

pentinized peridotite from the Franciscan Complex, California, and fresh mantle peridotite.

Interestingly, before the system reaches steady state with respect to pH, an increase in aSiO$_2$ and δ^{30}Si is observed (Fig. 4b). This increase in aSiO$_2$ was explained by Schlicht (2020) as an immediate reaction of a very fine-grained solid fraction upon exposure to the fluid early in the reaction progress. However, as the δ^{30}Si in the fluid increases, and assuming that Si isotope fractionation during mineral dissolution is negligible, precipitation of an early silica-rich phase must simultaneously occur at this stage. This counterintuitive observation (increasing aSiO$_2$ with increasing δ^{30}Si) was recently made in low-temperature environments (∼4 °C) during serpentine alteration on the seafloor – it was explained with simultaneous silica dissolution and Si re-precipitation reactions (Geilert et al., 2020b). Nonetheless the process resulted in an early net increase in fluid Si concentrations due to delayed Si precipitation. However, it is surprising to observe such a Si isotope shift at 300 °C, which indicates that rapid removal of Si during precipitation can induce Si isotope fractionation at high temperatures as well if the reaction is incomplete. Since the instantaneous precipitate could not be recovered during the ongoing experiments, a fractionation factor cannot be deduced.

6.3. Late veins (#3.1; high w/r): tracer of slab released fluids

Serpentine that formed during fluid-dominated conditions in late veins (#3.1) either has δ^{30}Si higher (on average −0.10‰ at Yinazao) or lower (−1.94‰ at Fantangisña and −0.80‰ and −0.93‰ at Asùt Tesoru) compared to unserpentinized olivine (Fig. 5). We interpret these values to provide information on the sources of the serpentinization fluid, since the alteration occurred at temperatures at which no significant Si fractionation is expected (i.e., Fig. 4c at T > 80 °C) and interactions between serpentinizing fluids and host minerals were rather limited (high w/r ratios). These sources are either marine sediments or oceanic crust; each feature distinct δ^{30}Si values. At the Mariana convergent margin, subducting sediments are mainly composed of deep sea clays and chert- and radiolarite-rich sediments (Plank and Langmuir, 1998).

Yinazao serpentine veins show the highest δ^{30}Si in #3.1 compared to the other mud volcanoes (Fig. 5). Marine sedimentary sources of relatively high δ^{30}Si values are pore fluids and radiolarian-rich sediments. Radiolarians yield δ^{30}Si averaging at about +1.5‰ (Hendry et al., 2014). However, upon burial and diagenesis, biogenic amorphous opal will transform to higher crystalline silica phases (e.g. opal-CT, quartz) potentially entailing a shift in isotope values and releasing a fractionated fluid (Tatzel et al., 2015; Geilert et al., 2016). Regardless, pore fluids from radiolaria-rich sediments will be characterized by δ^{30}Si that are controlled by the dissolution of biogenic silica and detrital minerals, and the precipitation of authigenic phases. Such pore fluids were found to range between −0.5 to +2.1‰ (Ehlert et al., 2016; Geilert et al., 2020a; Ng et al., 2020; Cassarino et al., 2021). This range encompasses the serpentine vein values of −0.10‰ and radiolarian sediments and their associated pore fluids are thus potential sources for Yinazao sediment dehydration at depth.

The lowest δ^{30}Si values (on average −1.94‰) were detected at Fantangisña. Marine sediments featuring such low δ^{30}Si are secondary minerals like clays (−2.16‰ to −0.11‰; Bayon et al., 2018). Thus, desilication of clay minerals represents the only source capable to create these low δ^{30}Si values. At the inferred slab temperature range below Fantangisña (∼150 °C; Mottl et al., 2004; Hulme et al., 2010), the smectite-illite desilication transition is likely to occur; liberating among other elements, Si and water (Środoń, 1999).

At Asùt Tesoru, δ^{30}Si is slightly higher than at Fantangisña (−0.80 and −0.93‰). Here, either clay minerals with higher δ^{30}Si
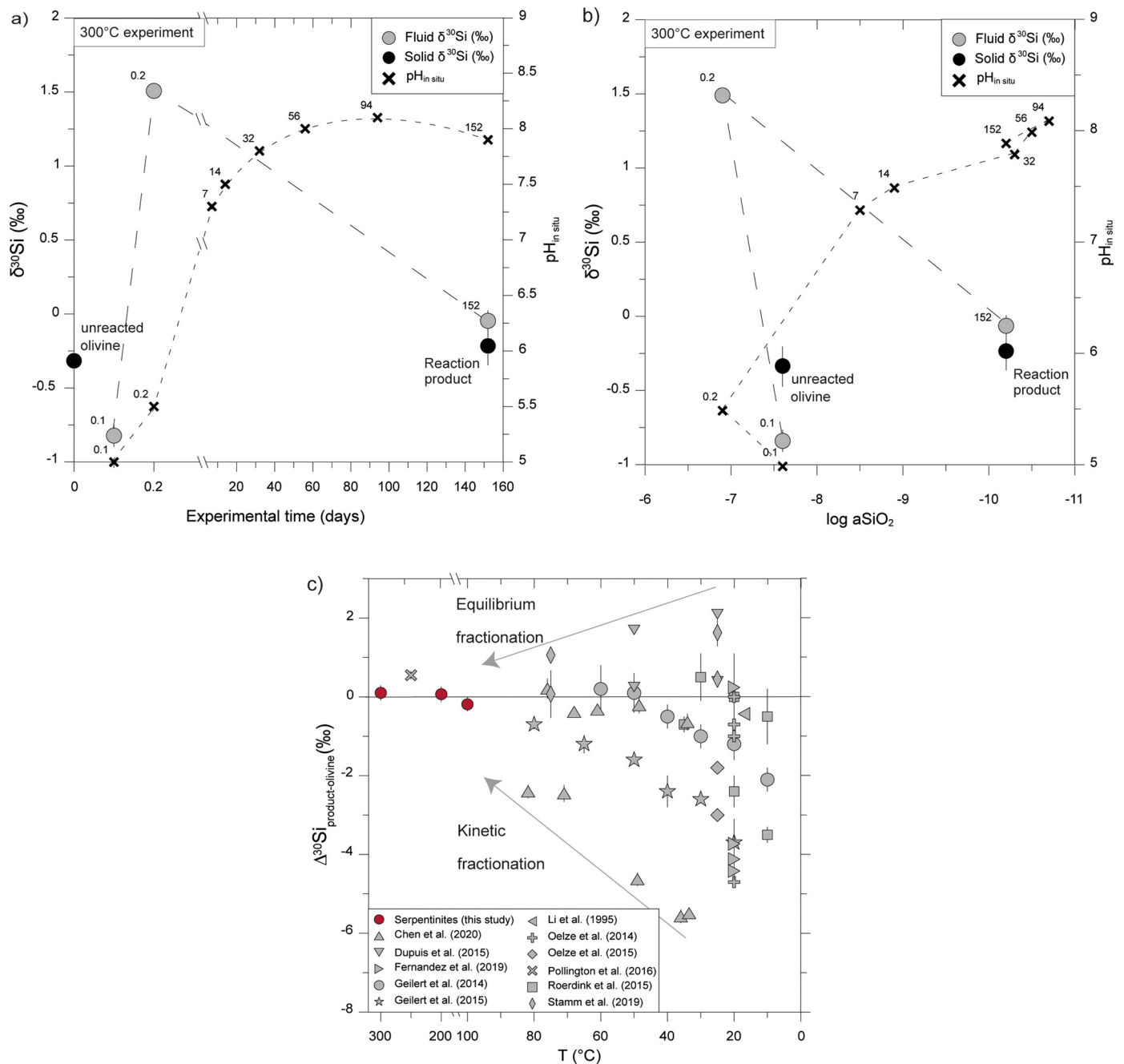
Fig. 4. Results of the serpentinization experiments. (a) δ^{30}Si and pH versus experimental time at 300°C. Labels indicate reaction time in days. (b) δ^{30}Si and pH versus aSiO$_2$ at 300°C. Labels indicate reaction time in days. Note that the aSiO$_2$ from 0.1 days is taken for unreacted olivine for graphic purposes. (c) Si isotope fractionation (Δ^{30}Si$_{product-olivine}$) versus temperature for serpentinization from experiments from this study and from the literature (Li et al., 1995; Geilert et al., 2014, 2015; Oelze et al., 2014; Dupuis et al., 2015; Oelze et al., 2015; Roerdink et al., 2015; Pollington et al., 2016; Fernandez et al., 2019; Stamm et al., 2019; Chen et al., 2020). The large range in Δ^{30}Si$_{product-olivine}$ is caused amongst others by differences in pH, precipitation rate, surface area, reaction time, presence of metals, and kinetic or equilibrium fractionation. Nevertheless, the general trend denotes decreasing Δ^{30}Si$_{product-olivine}$ with increasing temperature for both kinetic and equilibrium fractionation (horizonal line denotes no fractionation).

values dehydrate or an additional source adds to the observed isotope composition. Clay minerals show a distinct shift towards lighter Si isotope composition with increasing degree of crystallization, resulting in δ^{30}Si that are higher in low-crystalline clays like smectite in comparison to high-crystalline clays like kaolinite (Opfergelt et al., 2012). With respect to clay solubilities though, low-crystalline clays will dehydrate before high-crystalline clays (Gaboreau et al., 2020), so that in relation to the geographic location of the mud volcanoes, Fantangisña should be sourced by clays with high δ^{30}Si and Asùt Tesoru by clays with low δ^{30}Si. However,

this is opposite to the observed isotopic signatures of serpentine veins (Fig. 3, 5).

Another source of relatively high δ^{30}Si compared to clays is the subducting altered oceanic crust. The Si isotope composition of the altered oceanic crust is not well-constrained and the only direct measurement originates from the eastern side of the East Pacific Rise with δ^{30}Si of -0.32 ± 0.06‰ (Yu et al., 2018). This value is however indistinguishable from unaltered oceanic crust (-0.29 ± 0.08‰; Savage et al., 2010), likely due to the relatively low alteration degree ($\leq$10%; Alt et al., 2010). However, despite the limited data on altered oceanic crust, δ^{30}Si is higher than most clay
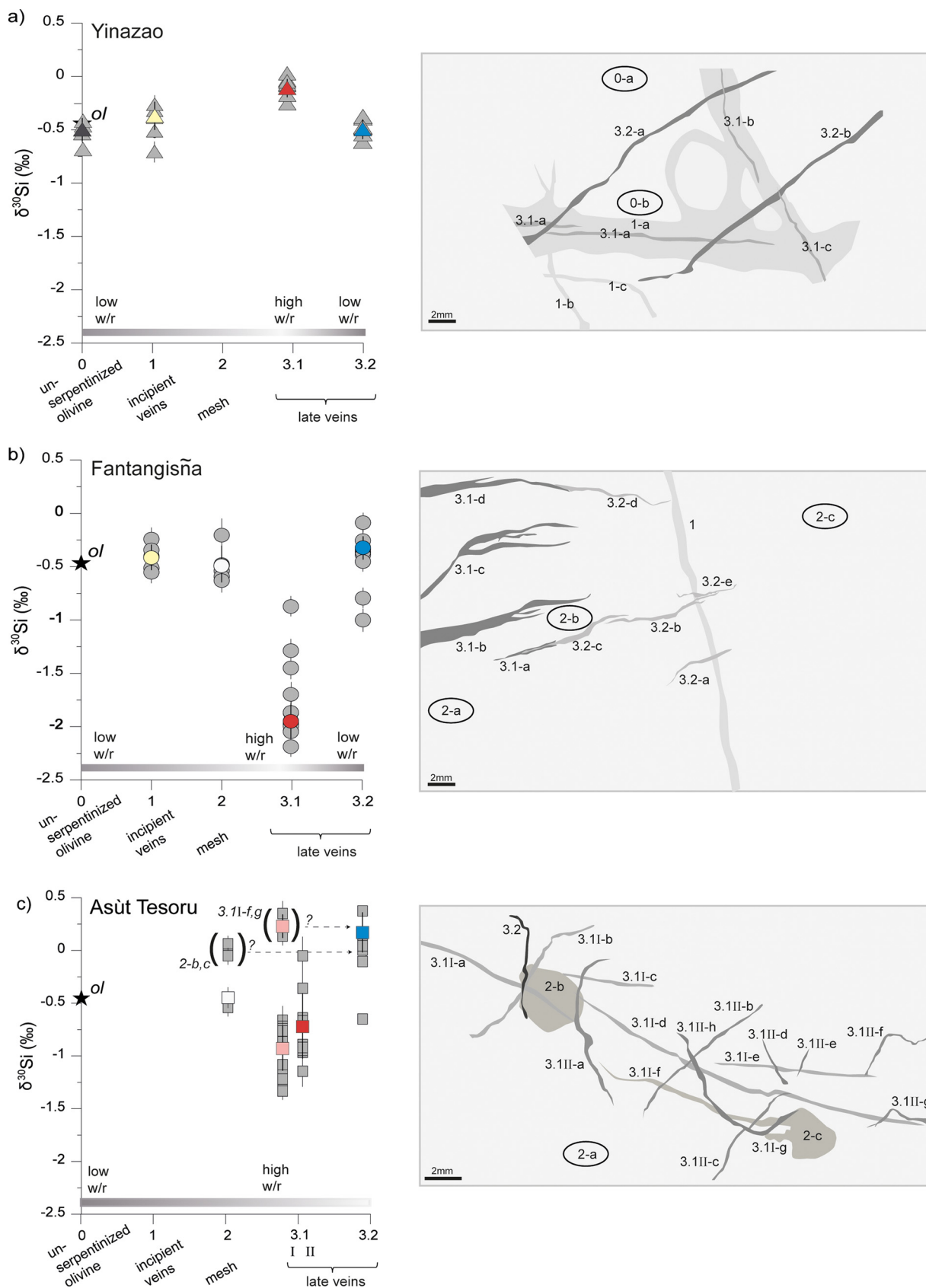
Fig. 5. Relationships between individual serpentine generations (#0 to 3, see section 5.1) and their isotopic composition in chronological order of their formation for (a) Yinazao, (b) Fantangisña, and (c) Asùt Tesoru. Grey symbols mark δ^{30}Si of individual line scans and colored symbols are averaged values for the respective generation (cf. Table 1, A.6). Sketches of the thin sections are shown for illustration (see Fig. 2 for thin section scans). Note that bastite serpentine and related veins at Asùt Tesoru (#2-b, #2-c, #3.1I-f, and #3.1I-g) cannot unambiguously assigned to a formation time on the basis of their diverging δ^{30}Si values (shift to higher values compared to the respective vein generations). Black stars mark average δ^{30}Si values of olivine (ol) (Savage et al., 2011).
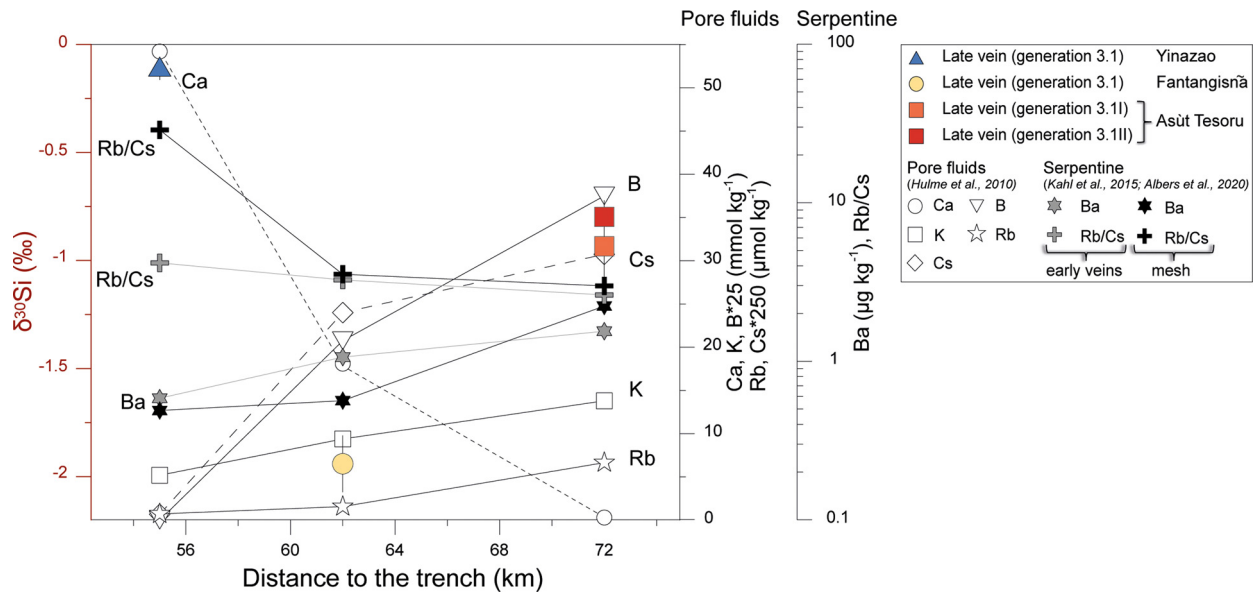
Fig. 6. Variations of average late vein (#3.1) Si isotopes in context with selected pore fluid and serpentine chemistry across the Mariana forearc in relative distance to the trench axis. Pore fluid chemistry from Mottl et al. (2004) and Hulme et al. (2010). Serpentine vein chemistry from Kahl et al. (2015) and Albers et al. (2020). With increasing distance to the trench, increasing B, Rb, Cs, K, Ba and decreasing Ca concentrations as well as decreasing Rb/Sr ratios were interpreted to reflect sediment compaction, carbonate dissolution, and opal diagenesis at 30 to 80 °C, clay diagenesis at 80 to 150 °C, and decomposition of clays and altered oceanic crust at >250 °C. These slab lithologies correspond well to high, low, and intermediate δ^{30}Si values, respectively.
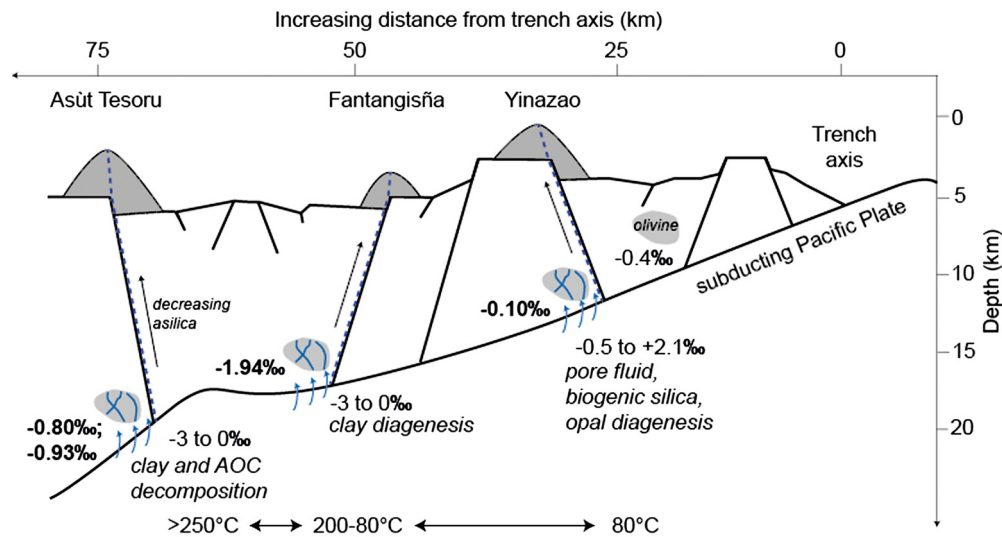
Fig. 7. Sketch of the Mariana forearc system and depth-related fluid liberation from the subducting slab. The fluids released from the slab carry distinct δ^{30}Si values across the forearc (fluid flow indicated with blue dotted lines and arrows) - these trends are mirrored in Si isotope compositions of forearc serpentine that formed under rather high w/r ratios. Our Si isotope data are suggestive of fluids originating from dominantly biogenic silica, opal diagenesis and pore fluid release underneath Yinazao, clay diagenesis at Fantangisña, and clay and altered oceanic crust (AOC) decomposition at Asùt Tesoru. See main text for details.

isotopic signatures and concurrent dissolution of clays and altered oceanic crust has the potential to shift Asùt Tesoru pore fluids to higher values compared to Fantangisña. The δ^{30}Si values of serpentine veins from Asùt Tesoru are thus interpreted to originate from the dehydration of clays and altered oceanic crust, which would source Si ranging from −2.16 to −0.11‰ (Bayon et al., 2018; Yu et al., 2018).

Across the forearc, we observe a trend in late vein serpentine (#3.1) δ^{30}Si that generally follows the isotopic compositions of the potential fluid sources below the individual mud volcanoes (Fig. 6, 7): late veins from Yinazao samples match those of sedimentary pore fluids, biogenic silica and opal diagenesis, those from Fantangisña are similar to fluids originating from clay dehydration, and those from Asùt Tesoru are reminiscent of clay and altered oceanic crust decomposition. We hence show that isotopic compo-

sitions of serpentine in fluid-dominated veins are indicative of the respective fluid source. Our *in situ* Si isotope measurements thus contrast those of bulk δ^{30}Si analyses of serpentinized peridotites by Wang et al. (2019), who claim that the δ^{30}Si of slab-derived fluids is similar to that of mantle peridotites. Our interpretations refine results inferred from geochemical variations in mud volcano pore fluids (Mottl et al., 2004; Hulme et al., 2010) and are in line with results from *in situ* fluid mobile element variations in serpentine veins, which indicated similar slab dehydration reactions (Fig. 6) (Albers et al., 2020). We infer that Si isotopes in serpentine that has formed under fluid-dominated conditions can be used as an additional proxy in addition to major and trace elements as well as fluid mobile element concentrations for slab dehydration reactions (Fig. 6, 7).

6.4. Late veins (#3.2): other processes affecting $\delta^{30}Si$

The latest vein generations (#3.2), however, deviate in their $\delta^{30}Si$ from the fluid derived signatures, as discussed above. Late-vein generations from Yinazao and Fantangisña, with $\delta^{30}Si$ of $-0.49‰$ and $-0.30‰$, respectively (#3.2; Fig. 5), formed under rock-dominated conditions due to pervasive fluid migration (low w/r ratios; section 5.1) and resemble in their isotopic composition the $\delta^{30}Si$ of the mesh and incipient serpentine veins. Thus, these veins inherited the $\delta^{30}Si$ of olivine, instead of adapting the slab-signature.

In contrast, late veins at Asùt Tesoru formed under fluid-dominated conditions with no direct interaction with the host rock (high w/r ratios; see section 5.1) and obtained a $\delta^{30}Si$ value of $+0.22‰$; much higher than the other fluid-dominated veins discussed in section 6.3 ($-0.93‰$ (#3.1I) and $-0.80‰$ (#3.1II)). If this vein does not originate from a yet unidentified fluid source of high $\delta^{30}Si$, its $\delta^{30}Si$ may have been affected by continued diagenetic and/or metamorphic processes in the subduction channel or by fractionation processes during rise of the fluids in the mud volcano conduit (cf. Kahl et al., 2015; Albers et al., 2020).

7. Significance of the serpentine $\delta^{30}Si$ proxy

The findings of this study show that $\delta^{30}Si$ in serpentine formed under high w/r ratios reliable record the different dehydration stages of slab sediments and crust and thus allows the identification of different slab mineral phases. However, the bulk mantle Si isotope composition is presumably not significantly impacted by serpentinization. The reason for this is that the extremely low or high $\delta^{30}Si$ values of late veins with high w/r ratios constitute only a small part of the ultramafic clasts (about 10%), whereas the bulk serpentinized rock (mesh and early veins; about 70 and 20%, respectively) has $\delta^{30}Si$ values similar to pristine olivine. This result agrees therefore well with the findings by Wang et al. (2019) who found that metasomatism by slab-derived fluids does not significantly change the bulk mantle Si isotope composition.

The newly established $\delta^{30}Si$ proxy though provides new opportunities to answer long-standing questions regarding dehydration reactions of the subducted slab, mantle hydration, composition of Archean granitoids and sediments, and in view of the Si cycle, might shed light on the question when silica biomineralizers evolved. The latter significantly affecting oceanic Si concentrations and further associated nutrients as well as CO_2, as especially diatoms are highly efficient carbon exporters (e.g. Sutton et al. (2018) and references therein). The evolution of oceanic Si concentrations was for a long time considered to be controlled by abiotic reactions in the Precambrian and a significant drop of oceanic Si concentrations only occurred with the rise of diatoms in the Cenozoic (Siever, 1992; Maliva et al., 2005). This concept was challenged in recent years with the finding that certain cyanobacteria, already present in the Precambrian, were capable of accumulating significant amounts of Si (Baines et al., 2012; Marron et al., 2016), potentially lowering oceanic Si concentrations since the Archean (Conley et al., 2017). However, the exact onset of silica biomineralization and thus the drop in oceanic Si concentrations is still unknown.

Independent of the exact onset of the evolution of silica biomineralizers, Archean seawater was likely close to Si saturation, facilitating the direct precipitation of silica-rich deposits like cherts, which constituted the largest proportion of Archean marine sediments (e.g. Maliva et al., 2005). Archean cherts have average $\delta^{30}Si$ values of about $+0.6‰$ (Stefurak et al., 2015 and references therein). Reworking of these sediments together with silicified seafloor basalts ($\delta^{30}Si = +0.43 \pm 0.14‰$; André et al.,

2019) have recently been found to have played a key role in creating Archean granitoids (André et al., 2019; Deng et al., 2019). These Archean models include partial melting of sediments and crust, which transferred the Si isotopic signal of reworked material into arc volcanic products such as granitoids (André et al., 2019; Deng et al., 2019). Dating back further, Si isotope data from 4.1 Ga old Hadean zircons as well as 3.75 Ga Archean zircons was also proposed to originate from melting of chemical sediments and serpentinized rocks (Trail et al., 2018; Chowdhury et al., 2020).

The use of the here established $\delta^{30}Si$ proxy has the capacity to unravel the open question related to the onset of silica biomineralization and test hypotheses of Archean crust formation and Hadean sedimentary inventories by investigating serpentine veins in ophiolites of ancient subduction systems. Such paleo-forearc serpentinites are for instance exposed in obducted rock sequences like the Californian Coast Ranges recording subduction processes 165 to 32 Ma years ago (e.g. Wakabayashi, 2017) or in the Archean Tartoq Group (SW Greenland) documenting potential subduction processes about 2.9 Ga years ago (Szilas et al., 2014). The $\delta^{30}Si$ in paleo-forearc serpentinites can be used to identify Archean crustal evolution and sedimentary composition and narrow down the onset of silica biomineralizers, clarifying oceanic nutrient and CO_2 cycling through geological time.

8. Conclusions

The Si isotope compositions of late serpentine veins formed under high w/r ratios in ultramafic clasts from the Mariana forearc mantle wedge mirror those of the dehydrating lithologies of the subducting slab. Lithologies identified during slab dehydration are 1) opal derived from the diagenesis of biogenic silica-rich sediments and associated pore fluids; 2) clay mineral dehydration; and 3) clay mineral and altered oceanic crust dehydration. Si isotopes can thus be used as a new proxy for slab dehydration processes, which may help to identify the type of subducted sediments in serpentine from paleo-forearc settings.

CRediT authorship contribution statement

SG conceptualized and planned the study. EA sailed research cruise IODP Exp. 366 and conducted the electron microprobe measurements. CTH performed the batch experiments. DAF conducted the laser ablation MC-ICPMS Si isotope measurements and together with FvB validated the data. SG measured Si isotopes in the experimental samples. SG and EA prepared the manuscript with the support of CTH, DAF, and FvB.

Declaration of competing interest

The authors declare that they have no known competing financial interests or personal relationships that could have appeared to influence the work reported in this paper.

Acknowledgements

Appendix A. Supplementary material

Supplementary material related to this article can be found online at https://doi.org/10.1016/j.epsl.2021.117193.

References

Albers, E., Kahl, W.-A., Beyer, L., Bach, W., 2020. Variant across-forearc compositions of slab-fluids recorded by serpentinites: implications on the mobilization of FMEs from an active subduction zone (Mariana forearc). Lithos 364–365, 105525.

Alt, J.C., Laverne, C., Coggon, R.M., Teagle, D.A.H., Banerjee, N.R., Morgan, S., Smith-Duque, C.E., Harris, M., Galli, L., 2010. Subsurface structure of a submarine hydrothermal system in ocean crust formed at the East Pacific Rise, ODP/IODP Site 1256. Geochem. Geophys. Geosyst. 11.

André, L., Abraham, K., Hofmann, A., Monin, L., Kleinhanns, I.C., Foley, S., 2019. Early continental crust generated by reworking of basalts variably silicified by seawater. Nat. Geosci. 12, 769–773. https://doi.org/10.1038/s41561-019-0408-5.

Bach, W., Paulick, H., Garrido, C.J., Ildefonse, B., Meurer, W.P., Humphris, S.E., 2006. Unraveling the sequence of serpentinization reactions: petrography, mineral chemistry, and petrophysics of serpentinites from MAR 15°N (ODP Leg 209, Site 1274). Geophys. Res. Lett. 33, 4–7.

Baines, S.B., Twining, B.S., Brzezinski, M.A., Krause, J.W., Vogt, S., Assael, D., Mc-Daniel, H., 2012. Significant silicon accumulation by marine picocyanobacteria. Nat. Geosci. 5, 886–891.

Bayon, G., Delvigne, C., Ponzevera, E., Borges, A.V., Darchambeau, F., De Deckker, P., Lambert, T., Monin, L., Toucanne, S., André, L., 2018. The silicon isotopic composition of fine-grained river sediments and its relation to climate and lithology. Geochim. Cosmochim. Acta 229, 147–161.

van den Boorn, S.H.J.M., Vroon, P.Z., van Belle, C.C., van der Wagt, B., Schwieters, J., van Bergen, M.J., 2006. Determination of silicon isotope ratios in silicate materials by high-resolution MC-ICP-MS using a sodium hydroxide sample digestion method. J. Anal. At. Spectrom. 21, 734.

Cassarino, L., Hendry, K.R., Henley, S.F., MacDonald, E., Arndt, S., Freitas, F.S., Pike, J., Firing, Y.L., 2021. Sedimentary nutrient supply in productive hot spots off the West Antarctic Peninsula revealed by silicon isotopes. Glob. Biogeochem. Cycles 34.

Chen, X., Chafetz, H.S., Lapen, T.J., 2020. Silicon isotope variations in hydrothermal systems at Yellowstone National Park, Wyoming, U.S.A.. In: GCA 283, pp. 184–200.

Chowdhury, W., Trail, D., Guitreau, M., Bell, E.A., Buettner, J., Mojzsis, S.J., 2020. Geochemical and textural investigations of the Eoarchean Ukaliq supracrustals, Northern Québec (Canada). Lithos 372-373, 105673. https://doi.org/10.1016/j.lithos.2020.105673.

Conley, D.J., Frings, P.J., Fontorbe, G., Clymans, W., Stadmark, J., Hendry, K.R., Marron, A.O., De La Rocha, C.L., 2017. Biosilicification drives a decline of dissolved si in the oceans through geologic time. Front. Mar. Sci. 4.

Debret, B., Albers, E., Walter, B., Price, R., Barnes, J., Beunon, H., Facq, S., Gilliken, D., Mattielli, N., Williams, H., 2019. Shallow forearc mantle dynamics and geochemistry: new insights from IODP expedition 366. Lithos 326–327, 230–245.

Deng, Z., Chaussidon, M., Guitreau, M., Puchtel, I.S., Dauphas, N., Moynier, F., 2019. An oceanic subduction origin for Archaean granitoids revealed by silicon isotopes. Nat. Geosci. 12, 774–778. https://doi.org/10.1038/s41561-019-0407-6.

Deschamps, F., Godard, M., Guillot, S., Hattori, K., 2013. Geochemistry of subduction zone serpentinites: a review. Lithos 178, 96–127.

Dupuis, R., Benoit, M., Nardin, E., Méheut, M., 2015. Fractionation of silicon isotopes in liquids: the importance of configurational disorder. Chem. Geol. 396, 239–254. Available at: http://linkinghub.elsevier.com/retrieve/pii/S0009254115000029.

Ehlert, C., Doering, K., Wallmann, K., Scholz, F., Sommer, S., Grasse, P., Geilert, S., Frank, M., 2016. Stable silicon isotope signatures of marine pore waters – biogenic opal dissolution versus authigenic clay mineral formation. Geochim. Cosmochim. Acta 191, 102–117. https://doi.org/10.1016/j.gca.2016.07.022.

Fernandez, N.M., Zhang, X., Druhan, J.L., 2019. Silicon isotopic re-equilibration during amorphous silica precipitation and implications for isotopic signatures in geochemical proxies. Geochim. Cosmochim. Acta 262, 104–127. https://doi.org/10.1016/j.gca.2019.07.029.

Frings, P.J., Clymans, W., Fontorbe, G., De La Rocha, C.L., Conley, D.J., 2016. The continental Si cycle and its impact on the ocean Si isotope budget. Chem. Geol. 425, 12–36. https://doi.org/10.1016/j.chemgeo.2016.01.020.

Frost, B.R., Beard, J.S., 2007. On silica activity and serpentinization. J. Petrol. 48, 1351–1368.

Fryer, P., Ambos, E.L., Hussong, D.M., 1985. Origin and emplacement of Mariana forearc seamounts (Pacific). Geology 13, 774–777.

Fryer, P., Wheat, C.G., Williams, T., Expedition 366 Scientists T., 2018. Mariana convergent margin and South Chamorro seamount. In: Proc. Int. Ocean Discov. Program, 366 Coll. Station. TX (International Ocean Discov. Program). Available at: https://doi.org/10.14379/iodp.proc.366.2018.

Gaboreau, S., Gailhanou, H., Blanc, P., Vieillard, P., Made, B., 2020. Clay mineral solubility from aqueous equilibrium: assessment of the measured thermodynamic properties. Appl. Geochem. 113, 104465.

Geilert, S., Grasse, P., Doering, K., Wallmann, K., Ehlert, C., Scholz, F., Frank, M., Schmidt, M., Hensen, C., 2020a. Impact of ambient conditions on the Si isotope fractionation in marine pore fluids during early diagenesis. Biogeosciences 17, 1745–1763.

Geilert, S., Grasse, P., Wallmann, K., Liebetrau, V., Menzies, C.D., 2020b. Serpentine alteration as source of high dissolved silicon and elevated δ30Si values to the marine Si cycle. Nat. Commun. 11.

Geilert, S., Vroon, P.Z., van Bergen, M.J., 2016. Effect of diagenetic phase transformation on the silicon isotope composition of opaline sinter deposits of Geysir, Iceland. Chem. Geol. 433.

Geilert, S., Vroon, P.Z., Keller, N.S., Gudbrandsson, S., Stefánsson, A., van Bergen, M.J., 2015. Silicon isotope fractionation during silica precipitation from hot-spring waters: evidence from the Geysir geothermal field, Iceland. Geochim. Cosmochim. Acta 164.

Geilert, S., Vroon, P.Z., Roerdink, D.L., Van, Cappellen P., van Bergen, M.J., 2014. Silicon isotope fractionation during abiotic silica precipitation at low temperatures: inferences from flow-through experiments. Geochim. Cosmochim. Acta 142, 95–114. Available at: http://linkinghub.elsevier.com/retrieve/pii/S0016703714004542.

Georg, R.B., Reynolds, B.C., Frank, M., Halliday, A.N., 2006. New sample preparation techniques for the determination of Si isotopic compositions using MC-ICPMS. Chem. Geol. 235, 95–104.

Hansen, C.T., Meixner, A., Kasemann, S.A., Bach, W., 2017. New insight on Li and B isotope fractionation during serpentinization derived from batch reaction investigations. Geochim. Cosmochim. Acta 217, 51–79. https://doi.org/10.1016/j.gca.2017.08.014.

Hendry, K.R., Robinson, L.F., McManus, J.F., Hays, J.D., 2014. Silicon isotopes indicate enhanced carbon export efficiency in the North Atlantic during deglaciation. Nat. Commun. 5, 1–9. https://doi.org/10.1038/ncomms4107.

Hulme, S.M., Wheat, C.G., Fryer, P., Mottl, M.J., 2010. Pore water chemistry of the Mariana serpentinite mud volcanoes: a window to the seismogenic zone. Geochem. Geophys. Geosyst. 11.

Hyndman, R.D., Peacock, S.M., 2003. Serpentinization of the forearc mantle. Earth Planet. Sci. Lett. 212, 417–432.

Kahl, W.-A., Jöns, N., Bach, W., Klein, F., Alt, J.C., 2015. Ultramafic clasts from the South Chamorro serpentine mud volcano reveal a polyphase serpentinization history of the Mariana forearc mantle. Lithos 227, 1–20. https://doi.org/10.1016/j.lithos.2015.03.015.

Kastner, M., Solomon, E.A., Harris, R.N., Torres, M.E., 2014. Fluid origins, thermal regimes, and fluid and solute fluxes in the forearc of subduction zones. In: Stein, R., Blackman, D.K., Inagaki, F., Larsen, H.-C. (Eds.), Earth and Life Processes Discovered from 947 Subseafloor Environments: a Decade of Science Achieved by the Integrated Ocean Drilling 948 Program (IODP). Elsevier, Amsterdam, pp. 671–733.

Li, Y., Tiping, D., Defang, W., 1995. Experimental study of silicon isotope dynamic fractionation and its application in geology. Chin. J. Geochem. 14, 212–219.

Maliva, R.G., Knoll, A.H., Simonson, B.M., 2005. Secular change in the Precambrian silica cycle: insights from chert petrology. Bull. Geol. Soc. Am. 117, 835–845.

Marron, A.O., Ratcliffe, S., Wheeler, G.L., Goldstein, R.E., King, N., Not, F., De, Vargas C., Richter, D.J., 2016. The evolution of silicon transport in Eukaryotes. Mol. Biol. Evol. 33, 3226–3248.

Mottl, M.J., Wheat, C.G., Fryer, P., Gharib, J., Martin, J.B., 2004. Chemistry of springs across the Mariana forearc shows progressive devolatilization of the subducting plate. Geochim. Cosmochim. Acta 68, 4915–4933.

Ng, C.H., Cassarino, L., Pickering, R.A., Woodward, E.M.S., Hammond, S.J., Hendry, K.R., 2020. Sediment efflux of silicon on the Greenland margin and implications for the marine silicon cycle. Earth Planet. Sci. Lett. 529, 115877. https://doi.org/10.1016/j.epsl.2019.115877.

Oakley, A.J., Taylor, B., Fryer, P., Moore, G.F., Goodliffe, A.M., Morgan, J.K., 2007. Emplacement, growth, and gravitational deformation of serpentinite seamounts on the Mariana forearc. Geophys. J. Int. 170, 615–634.

Oelze, M., von Blanckenburg, F., Bouchez, J., Hoellen, D., Dietzel, M., 2015. The effect of Al on Si isotope fractionation investigated by silica precipitation experiments. Chem. Geol. 397, 94–105. Available at: http://linkinghub.elsevier.com/retrieve/pii/S0009254115000078.

Oelze, M., von Blanckenburg, F., Hoellen, D., Dietzel, M., Bouchez, J., 2014. Si stable isotope fractionation during adsorption and the competition between kinetic and equilibrium isotope fractionation: implications for weathering systems. Chem. Geol. 380, 161–171. https://doi.org/10.1016/j.chemgeo.2014.04.027.

Opfergelt, S., Georg, R.B., Delvaux, B., Cabidoche, Y.M., Burton, K.W., Halliday a, N., 2012. Silicon isotopes and the tracing of desilication in volcanic soil weathering sequences, Guadeloupe. Chem. Geol. 326–327, 113–122. https://doi.org/10.1016/j.chemgeo.2012.07.032.

Plank, T., Langmuir, C.H., 1998. The chemical composition of subducting sediment and its consequences for the crust and mantle. Chem. Geol. 145, 325–394.

Pollington, A.D., Kozdon, R., Anovitz, L.M., Georg, R.B., Spicuzza, M.J., Valley, J.W., 2016. Experimental calibration of silicon and oxygen isotope fractionations be-

tween quartz and water at 250 ° C by in situ microanalysis of experimental products and application to zoned low δ 30 Si quartz overgrowths. Chem. Geol. 421, 127–142. https://doi.org/10.1016/j.chemgeo.2015.11.011.

Roerdink, D.L., van den Boorna, S.H.J.M., Geilert, S., Vroon, P.Z., van Bergen, M.J., 2015. Experimental constraints on kinetic and equilibrium silicon isotope fractionation during the formation of non-biogenic chert deposits. Chem. Geol. 402, 40–51. Available at: http://linkinghub.elsevier.com/retrieve/pii/S0009254115001205.

Savage, P.S., Georg, R.B., Armytage, R.M.G., Williams, H.M., Halliday, A.N., 2010. Silicon isotope homogeneity in the mantle. Earth Planet. Sci. Lett. 295, 139–146. https://doi.org/10.1016/j.epsl.2010.03.035.

Savage, Paul S., Georg, R.B., Williams, H.M., Burton, K.W., Halliday, A.N., 2011. Silicon isotope fractionation during magmatic differentiation. Geochim. Cosmochim. Acta 75, 6124–6139. https://doi.org/10.1016/j.gca.2011.07.043.

Schlicht, L.E.M., 2020. Isotopic signatures in seafloor hydrothermal systems: from crust creation to subduction. PhD thesis. University of Bremen.

Schuessler, J.A., Von Blanckenburg, F., 2014. Testing the limits of micro-scale analyses of Si stable isotopes by femtosecond laser ablation multicollector inductively coupled plasma mass spectrometry with application to rock weathering. Spectrochim. Acta, Part B, At. Spectrosc. 98, 1–18. https://doi.org/10.1016/j.sab.2014.05.002.

Schwarzenbach, E.M., Caddick, M.J., Beard, J.S., Bodnar, R.J., 2016. Serpentinization, element transfer, and the progressive development of zoning in veins: evidence from a partially serpentinized harzburgite. Contrib. Mineral. Petrol. 171, 1–22.

Siever, R., 1992. The silica cycle in the Precambrian. Geochim. Cosmochim. Acta 56, 3265–3272.

Środoń, J., 1999. Nature of mixed-layer clays and mechanisms of their formation and alteration. Annu. Rev. Earth Planet. Sci. 27, 19–53.

Stamm, F.M., Zambardi, T., Chmeleff, J., Schott, J., Von Blanckenburg, F., Oelkers, E.H., 2019. The experimental determination of equilibrium Si isotope fractionation factors among $H_4SiO_4°$, H_3SiO_4- and amorphous Silica ($SiO_2 \cdot 0.32\ H_2O$) at 25 and 75 °C using the three-isotope method. Geochim. Cosmochim. Acta 255, 49–68.

Stefurak, E.J.T., Fischer, W.W., Lowe, D.R., 2015. Texture-specific Si isotope variations in Barberton Greenstone Belt cherts record low temperature fractionations in early Archean seawater. Geochim. Cosmochim. Acta 150, 26–52. Available at: http://linkinghub.elsevier.com/retrieve/pii/S001670371400684X.

Sutton, J.N., André, L., Cardinal, D., Conley, D.J., de Souza, G.F., Dean, J., Dodd, J., Ehlert, C., Ellwood, M.J., Frings, P.J., Grasse, P., Hendry, K., Leng, M.J., Michalopoulos, P., Panizzo, V.N., Swann, G.E.A., 2018. A review of the stable isotope biogeochemistry of the global silicon cycle and its associated trace elements. Front. Earth Sci. 5. Available at: http://journal.frontiersin.org/article/10.3389/feart.2017.00112/full.

Szilas, K., Van Hinsberg, V.J., Creaser, R.A., Kisters, A.F.M., 2014. The geochemical composition of serpentinites in the Mesoarchean Tartoq Group, SW Greenland: Harzburgitic cumulates or melt-modified mantle? Lithos 198–199, 103–116.

Tatzel, M., von Blanckenburg, F., Oelze, M., Schuessler, J.A., Bohrmann, G., 2015. The silicon isotope record of early silica diagenesis. Earth Planet. Sci. Lett. 428, 293–303. https://doi.org/10.1016/j.epsl.2015.07.018.

Trail, D., Boehnke, P., Savage, P.S., Liu, M.-C., Miller, M.L., Bindeman, I., 2018. Origin and significance of Si and O isotope heterogeneities in Phanerozoic, Archean, and Hadean zircon. Proc. Natl. Acad. Sci. USA 115, 10287–10292.

Tréguer, P.J., Sutton, J.N., Brzezinski, M., Charette, M.A., Devries, T., Dutkiewicz, S., Ehlert, C., Hawkings, J., Leynaert, A., Liu, S.M., Llopis Monferrer, N., López-Acosta, M., Maldonado, M., Rahman, S., Ran, L., Rouxel, O., 2021. Reviews and syntheses: the biogeochemical cycle of silicon in the modern ocean. Biogeosciences 18, 1269–1289.

Wakabayashi, J., 2017. Serpentinites and serpentinites: variety of origins and emplacement mechanisms of serpentinite bodies in the California Cordillera. Isl. Arc 26.

Wang, B., Li, W.-Y., Deng, G., Huang, F., Yu, H.-M., 2019. Silicon isotope compositions of metaperidotites from the Franciscan Complex of California- implications for Si isotope fractionation during subduction dehydration. Lithos 350–351, 105228. https://doi.org/10.1016/j.lithos.2019.105228.

Yu, H.-M., Li, Y.-H., Gao, Y.-J., Huang, J., Huang, F., 2018. Silicon isotopic compositions of altered oceanic crust: Implications for Si isotope heterogeneity in the mantle. Chem. Geol. 479, 1–9.